Journal of Hazardous Materials 453 (2023) 131385

Contents lists available at ScienceDirect

Journal of Hazardous Materials

journal homepage: www.elsevier.com/locate/jhazmat

Dittmarite-type magnesium phosphates for highly efficient capture of Cs^+

Zeqiu Li, Chenyang Yang, Kuk Cho *

Department of Environmental Engineering, Pusan National University, 2 Busandaehak-ro, 63beon-gil, Geumjeong-gu, Busan 46241, Republic of Korea

HIGHLIGHTS

- Two dittmarite-type adsorbents, KMP and NMP, were synthesized.
- The Cs^+ adsorption capacities of KMP and NMP are 630 and 711 mg g^{-1}, respectively.
- KMP and NMP transformed into struvite-type $CsMgPO_4{\cdot}6H_2O$ (CsMP) after adsorption.
- CsMP has two structural forms, cubic or hexagonal, depending on the solution pH.

GRAPHICAL ABSTRACT

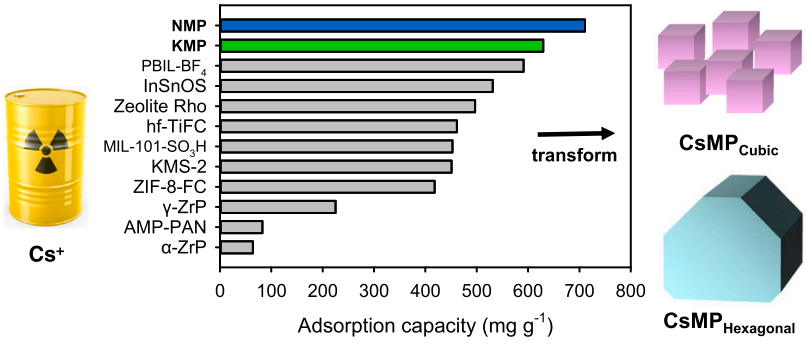

ARTICLE INFO

Editor: Arturo J Hernandez-Maldonado

Keywords:
Adsorption
Ion exchange
Radioactive
Caesium
Struvite

ABSTRACT

The presence of cesium ions (Cs^+) in radioactive wastewater has attracted considerable attention owing to their extreme toxic effects. Thus, there is an urgent need to develop adsorbents for Cs^+ with high adsorption capacities (q). While phosphate-based adsorbents have advantages for their disposal, previous adsorbents have shown limited q because of their limited capacity for ion exchange, despite showing high theoretical q values. In this study, two dittmarite-type magnesium phosphates, $KMgPO_4{\cdot}H_2O$ (KMP) and $NH_4MgPO_4{\cdot}H_2O$ (NMP), were synthesized because of their ability to contain readily exchangeable cations in their interlayers. KMP and NMP demonstrated remarkable adsorption capacities for Cs^+ (q_e^{KMP} = 630 mg g^{-1} and q_e^{NMP} = 711 mg g^{-1}), which were the highest among all reported adsorbents and are ~84 % of their theoretical values. Their distribution coefficients in waters with high divalent ion concentrations were low, which limits their use for the adsorption of Cs^+ from such environments. After adsorption, KMP and NMP were structurally transformed into struvite-type $CsMgPO_4{\cdot}6H_2O$ (CsMP), which has two different stacking structures, either cubic or hexagonal, depending on the pH of the solution. The high q values of KMP and NMP enable them to reduce the volume of radioactive waste for disposal.

Environmental implication

$^{137}Cs^+$ is a popular radionuclide generated from nuclear power plants, and the volume of its waste must be minimized for disposal. To minimize the volume, the adsorbent with higher adsorption capacity is advantageous. In this study, two dittmarite-type magnesium phosphates (KMP and NMP) were successfully

* Corresponding author.
E-mail address: kukcho@pusan.ac.kr (K. Cho).

https://doi.org/10.1016/j.jhazmat.2023.131385
Received 29 January 2023; Received in revised form 24 March 2023; Accepted 6 April 2023
Available online 7 April 2023

synthesized and used to remove Cs^+ from aqueous solutions. The highest adsorption capacities of KMP and NMP measured experimentally were 630 mg g^{-1} and 711 mg g^{-1}, respectively, which are the highest among all reported adsorbents. These high adsorption capacities will help to reduce the volume of Cs^+ wastes for disposal.

Data availability

Data will be made available on request.

1. Introduction

Cesium isotope ^{137}Cs is a common and dangerous nuclear fission product with a half-life of 30.2 years that can produce high-energy beta and gamma rays [19]. Cs^+ is water-soluble and behaves biologically like potassium ions [5]. Once ^{137}Cs enters the aquatic environment, it can cause ecological pollution and even serious diseases in humans, including cancer, leukemia, and genetic disorders [35,51]. Thus, the safe management and disposal of ^{137}Cs is critical for environmental safety, human health, and the development of the nuclear industry.

Phosphates have attracted growing interest for their radionuclide immobilization and adsorption owing to their high radiation resistance and chemical durability after vitrification [47]. Considering the solubility of phosphate salts, the divalent ions Sr(II) and Co(II) can react with phosphate ions (PO_4^{3-}) to form precipitates, such as $Sr_3(PO_4)_2$ ($K_{sp} = 1.0 \times 10^{-31}$) and $Co_3(PO_4)_2$ ($K_{sp} = 2.05 \times 10^{-35}$) [17,29,46]. However, phosphate cannot precipitate with the monovalent alkali metal ion Cs(I), which is found at the highest concentration remaining among various radionuclides after the Fukushima nuclear power plant accident [16]. As a result, Cs^+ must be removed from the water using the method other than precipitation.

Adsorption is a promising technology for separating Cs^+ on a large scale because of its simple operation, cost-effectiveness, and low level of secondary pollution [2]. To date, various phosphate adsorbents have been synthesized and used to adsorb Cs^+ from aqueous solutions, including ammonium molybdophosphate (AMP, $(NH_4)_3P(Mo_3O_{10})_4 \bullet 3H_2O$), α-zirconium phosphate (α-ZrP, $Zr(HPO_4)_2 \bullet H_2O$), and γ-zirconium phosphates (γ-ZrP, $Zr(PO_4)(H_2PO_4) \cdot 2H_2O$). AMP is an adsorbent that uses ion exchange between NH_4^+ and Cs^+; however, its non-layered crystal structure limits its adsorption capacity (139 mg g^{-1}) [11]. Even though α-ZrP and γ-ZrP have a layered structure and a high theoretical ion exchange capacity, their adsorption capacity for Cs^+ is lower than 225 mg g^{-1} [8,23,38,39] because this relies on the dissociation constant of phosphoric acid [8]. Although the synthesis of a phosphate-based adsorbent with a high adsorption capacity for Cs^+ is highly desirable, this remains a challenge.

Dittmarite-type phosphates are good candidates for Cs^+ adsorption owing to their layered structure and easily exchangeable ions, such as K^+ [20]. However, they have not been applied for adsorption, but rather for other applications, such as in the production of fertilizers [52], magnetic devices [53], supercapacitors [44] and precursors for phospho-olivine electrodes [20,22]. KMP ($KMgPO_4 \cdot H_2O$) and NMP ($NH_4MgPO_4 \cdot H_2O$), which are dittmarite-type compounds, have a theoretical adsorption capacity of 754 mg g^{-1} and 856 mg g^{-1} for Cs^+, respectively. Therefore, the application of KMP and NMP to Cs^+ adsorption is a meaningful and valuable research prospect.

In this study, KMP and NMP were prepared using a one-pot hydrothermal method. The crystals of the synthesized samples were confirmed to be dittmarite. Notably, KMP and NMP exhibited high adsorption capacities for Cs^+ (630 mg g^{-1} and 711 mg g^{-1}, respectively), which were much higher than those of previously reported adsorbents and are ~84 % of their theoretical values. After ion exchange, crystal transformation to struvite-Cs, $CsMgPO_4 \cdot 6H_2O$ (CsMP) took place. The crystal transformation was affected by the pH of the solution, resulting in CsMPs having two types of structures: $CsMP_{cubic}$ and $CsMP_{hexagonal}$. This study highlights the value of dittmarite-type magnesium phosphate and its significant potential as a radioactive Cs^+ adsorbent for environmental remediation.

2. Material and methods

Detailed descriptions of the reagents and characterization equipment are provided in the Supplementary Information. Unless specified otherwise, all chemical reagents were purchased from commercial sources and were used without further purification.

2.1. Preparation of $KMgPO_4 \cdot H_2O$ (KMP) and $NH_4MgPO_4 \cdot H_2O$ (NMP)

KMP was synthesized using $Mg(OH)_2$ (10 mmol, 0.61 g), K_2HPO_4 (25 mmol, 4.40 g), and deionized water (10 mL). NMP was synthesized by mixing $Mg(OH)_2$ (10 mmol, 0.61 g), $(NH_4)_2HPO_4$ (15 mmol, 2.01 g), and deionized water (10 mL). The each resulting mixture was added to a 100-mL Teflon-lined autoclave. The autoclave was then heated for 24 h at 150 °C before cooling to ambient temperature. After washing three times with deionized water and ethanol, the final white precipitate was collected using centrifugation, dried in a vacuum oven at 60 °C for 24 h, and stored for further use (yield of KMP: 1.66 g, 94.16 % based on Mg; yield of NMP: 1.34 g, 86.19 % based on Mg).

2.2. Batch adsorption experiments

Cs(I) model solutions of various concentrations were prepared by dissolving Cs^+ in deionized water. First, $CsNO_3$ was added to deionized water and stirred to prepare an artificial wastewater solution with the desired concentration of Cs^+ ions. Then, 20 mg of KMP or NMP was added to 20 mL of Cs^+ solution in a 30-mL glass vial. Finally, the reaction mixture was mechanically shaken at 150 rpm on an orbital shaker.

The adsorption capacity (q_e, mg g^{-1}), removal percentage (R, %), and distribution coefficient (K_d, mL g^{-1}) were calculated separately using Eqs. (1), (2), and (3):

$$q_e = \frac{C_o - C_e}{m} \times V \tag{1}$$

$$R(\%) = \frac{C_o - C_e}{C_o} \times 100 \tag{2}$$

$$K_d = \frac{C_o - C_e}{C_e} \times \frac{V}{m} \times 1000 \tag{3}$$

where C_o (mg L^{-1}) represents the initial concentration, C_e (mg L^{-1}) represents the equilibrium concentration of Cs^+ in the aqueous solution, V (mL) represents the volume of the cesium ion solution, and m (mg) represents the weight of the adsorbent.

To evaluate the influence of solution pH on Cs^+ adsorption, the pH of the solution was changed to pH 3, 5, 7, 9, and 11 using either 0.5 M HCl or 0.5 M NaOH solutions.

The effect of coexisting ions on the adsorption performance was examined by adding 10 mM Na^+ ($NaNO_3$), K^+ (KNO_3), Mg^{2+} ($Mg(NO_3)_2 \bullet 6H_2O$), or Ca^{2+} ($Ca(NO_3)_2 \bullet 4H_2O$) to a 500 mg L^{-1} Cs^+ solution.

2.3. Analysis

After conducting the adsorption tests, the liquid samples were filtered through a 0.22-μm Superfil Syringe filter (HK-CA20421) (PVDF membrane, hydrophilic) and diluted in an aqueous solution that included 0.2 % K^+ (KCl) and 2.5 % HNO_3. Finally, a flame atomic absorption spectrometer was used to measure the cesium ion concentration.

3. Results

3.1. Characterization and properties of KMP and NMP

The effect of the molar ratio of the phosphate precursors to Mg on the Cs^+ adsorption capacity was investigated. Fig. S1**(a)** and **(b)** showed the X-ray diffraction (XRD) patterns of KMP and NMP synthesized with different molar ratios of $Mg(OH)_2$: phosphate, while Fig. S1**(c)** showed a comparison of the adsorption capacities for Cs^+. The results showed that KMP and NMP had the highest Cs^+ adsorption capacities at the ratios of 2.5 and 1.5, and that their XRD patterns matched closely with the published $KMgPO_4{\cdot}H_2O$ (ICDD: 01–089–6348) and $NH_4MgPO_4{\cdot}H_2O$ (ICDD: 00–003–0028), respectively (Fig. 1**(a)**). These results indicate that KMP and NMP were successfully synthesized. Their corresponding crystal structures are shown in Fig. 1**(c)** and **(d)**. The characteristic Bragg peaks of KMP and NMP indicated their interlayer spacings of 8.15 Å and 8.59 Å, respectively.

The Fourier-transform infrared spectroscopy (FTIR) spectra of KMP and NMP, shown in Fig. 1**(b)**, were in accordance with a previous study [50]. The broad bands at 3373–3391 cm^{-1} belonged to O−H stretching vibrations, while the weaker peaks at 1695 cm^{-1}, 1659 cm^{-1}, 1470 cm^{-1}, and 1464 cm^{-1} were assigned to O−H bending vibrations [41]. For NMP, the extra peak at 1427 cm^{-1} compared to that of KMP was caused by the interaction between NH_4^+ and H_2O [50]. Moreover, the bands between 1031 and 939 cm^{-1} were caused by P−O stretching vibrations, and the bands between 567 and 629 cm^{-1} were the result of O−P−O bending vibrations [21].

The morphologies of KMP and NMP were observed using a field emission scanning electron microscope (FE-SEM). According to Fig. 1**(e)** and **(f)**, both KMP and NMP exhibited plate-like particle morphologies with an average edge length of 2 − 10 μm, similar to the morphologies of dittmarite-type compounds such as $KMnPO_4{\cdot}H_2O$ [20] and $NH_4MgPO_4{\cdot}H_2O$ [62], respectively.

Thermal analysis of the curve showed that the weight loss of KMP

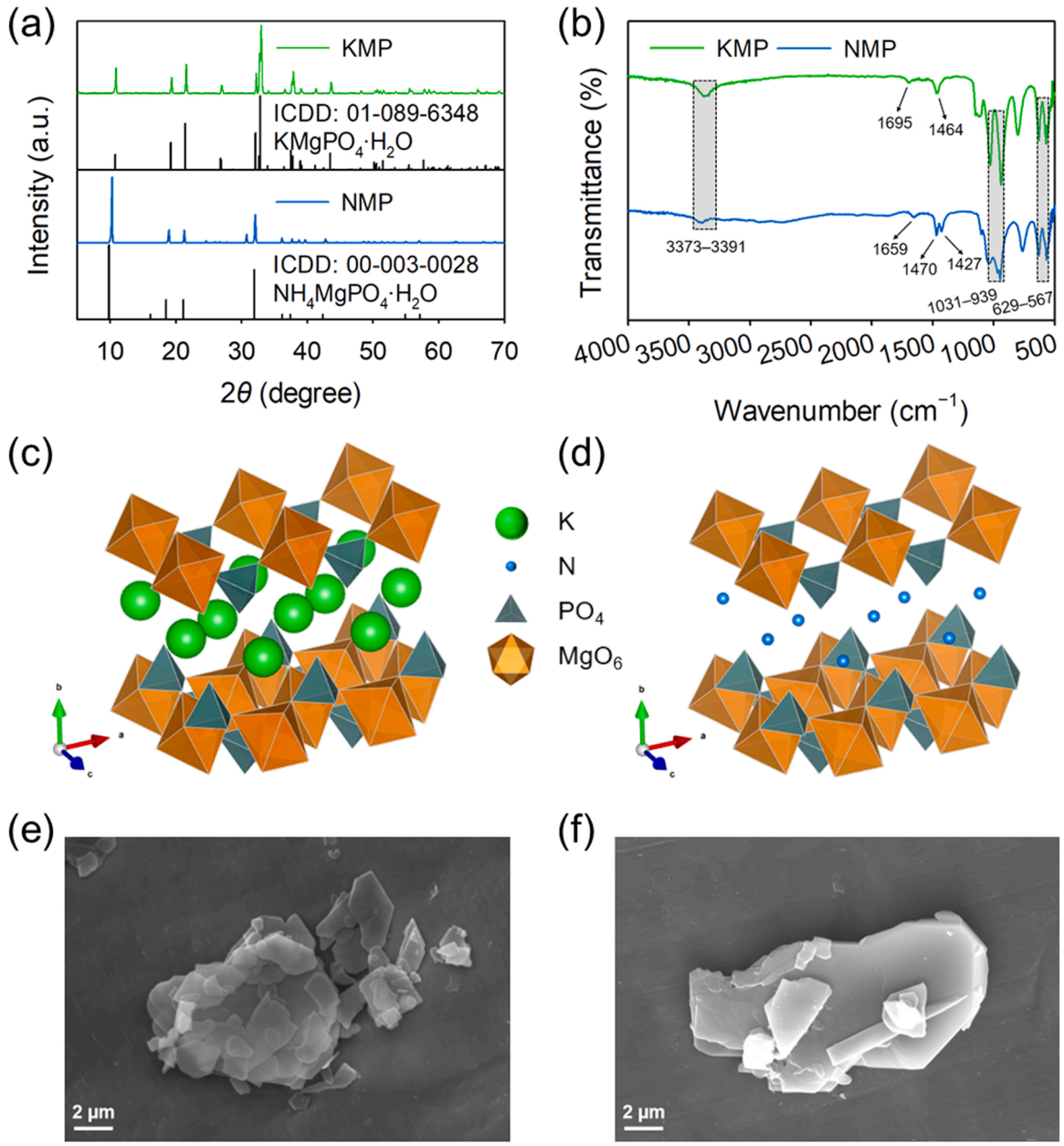

Fig. 1. (a) XRD patterns of KMP and NMP. (b) FTIR spectra of KMP and NMP. Crystal structure of (c) KMP and (d) NMP, which were drawn using VESTA (ver. 3.5.5) [37] with CIF [3,54]. FE-SEM images of (e) KMP and (f) NMP.

(2.0 %) and NMP (2.5 %) before 120 °C was mainly because of the evaporation of surface adsorbed water (Fig. S2). The weight loss between 120−800 °C was attributed to the evaporation of crystal water and the decomposition of ammonia molecules from the structure. The theoretical weight losses of KMP and NMP (10.2 % and 28.3 %) matched well with their experimental weight losses of them (10.2 % and 28.9 %).

The porosity and specific surface area of KMP and NMP were evaluated using the Brunauer-Emmett-Teller (BET) method. As delineated in Fig. S3, the nitrogen adsorption-desorption isotherms of KMP and NMP were typical type IV adsorption isotherms, and their respective BET surface areas were 3 and 1 $m^2\ g^{-1}$. In addition, the lack of a hysteresis loop indicated that they were low porous materials.

3.2. Cs^+ adsorption performances of KMP and NMP

3.2.1. Adsorption kinetics

To evaluate the adsorption kinetics of KMP and NMP, the effects of the contact time on Cs^+ adsorption were determined (Fig. 2**(a)** and **(b)**). KMP and NMP reached their adsorption equilibria at 240 min (R = 62.7 %) and 1440 min (R = 68.0 %), respectively. The removal kinetics of KMP and NMP for Cs^+ were comparable to those of some phosphate materials, including B-ZrP (t_e = 90 min) [38], DB-ZrP (t_e = 240 min) [39], and AMP^-PAN beads (t_e = 1440 min) [11]. However, the adsorption kinetics were slower than those of other materials, such as KMS-1 (t_e = 5 min, C_o = 1 mg L^{-1}) [33] and hf-TiFC (t_e = 5 min, C_o = 68 mg L^{-1}) [59]. The slower kinetics of NMP compared to that of KMP may be because of the hydrogen bonding between NH_4^+ and PO_4^{3-} in addition to electrostatic interactions [6].

3.2.2. Adsorption isotherms

The equilibrium adsorption capacity (q_e) was determined by measuring adsorption capacities at various concentrations. The highest q_e values of KMP and NMP for Cs^+ reached 630 mg g^{-1} and 711 mg g^{-1}, respectively (Fig. 2 **(c)** and **(d)**). Three nonlinear adsorption isotherm models (Langmuir, Freundlich, and Sips) were employed to match the Cs^+ adsorption data. The Sips model for KMP (r^2 = 0.983) and NMP (r^2 = 0.976) had a higher correlation coefficient than the Langmuir and Freundlich models, which implies that multilayer adsorption of Cs^+ occurred (Table 1). The maximum Sips adsorption capacities (q_m) of KMP and NMP for Cs^+ were determined to be 616 mg g^{-1} and 762 mg g^{-1}, respectively.

3.2.3. pH stability and coexisting ions

Given that radioactive wastewater can be either acidic or alkaline, the effect of the solution pH on the K_d values of Cs^+ was examined at various pH ranges (3−11). As shown in Fig. 3**(a)**, KMP and NMP maintained the K_d values from 5.0 × 10^4 to 5.4 × 10^4 mL g^{-1} and from 8.2 × 10^3 to 8.6 × 10^3 mL g^{-1} from pH 5–9, respectively. When the pH

Table 1
Adsorption isotherm parameters of Cs^+ on KMP and NMP obtained by fitting with different models.

Model	Parameter	Adsorbent	
		KMP	NMP
Langmuir	q_m (mg g^{-1})	669	913
	K_L (L mg^{-1})	0.106	0.017
	r^2	0.828	0.924
Freundlich	K_F (mg g^{-1}(L $mg^{-1})^{1/n}$)	197	76.8
	n_F	4.76	2.44
	r^2	0.648	0.800
Sips	q_m (mg g^{-1})	616	762
	K_S (L $mg^{-1})^n$	0.003	0.0005
	n_S	0.36	0.48
	r^2	0.983	0.976

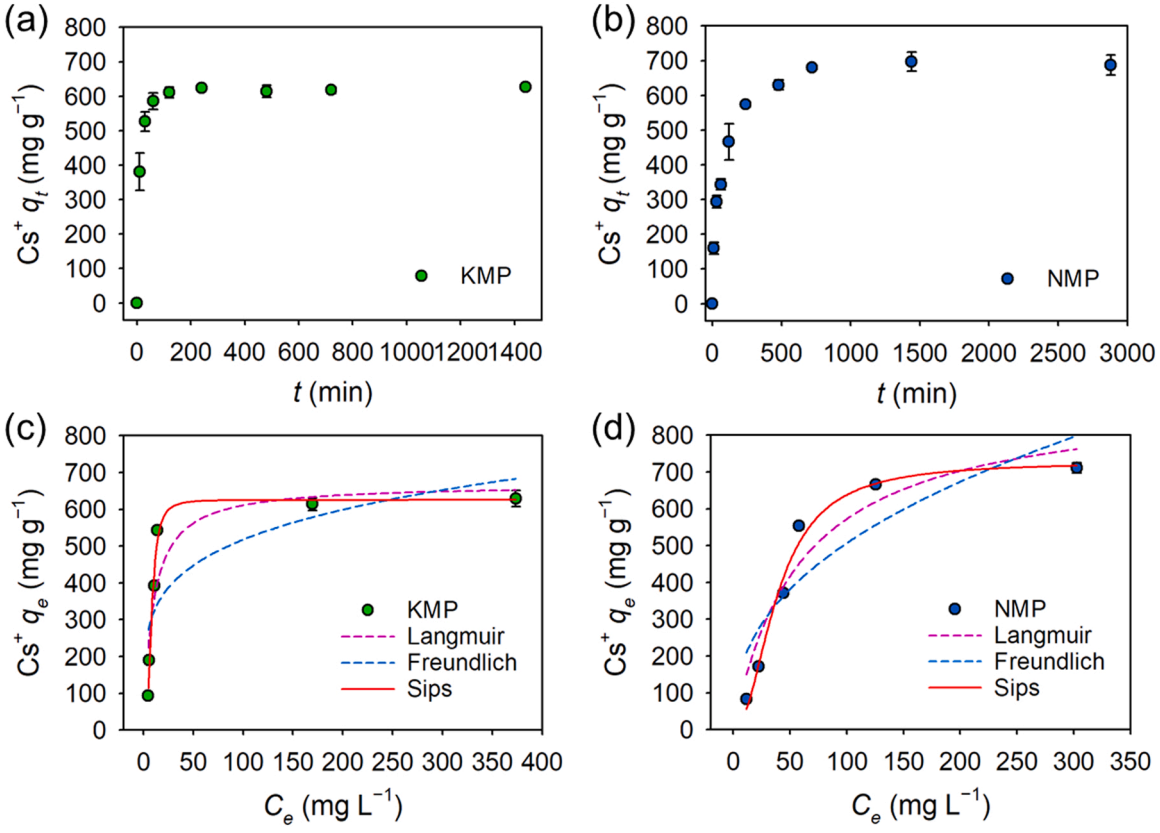

Fig. 2. Kinetics study for the removal of Cs^+ by (a) KMP and (b) NMP ($C_o \cong$ 1000 mg L^{-1}), and adsorption isotherms for Cs^+ by (c) KMP and (d) NMP and fittings by various isotherm models (t_{KMP} = 240 min, t_{NMP} = 1440 min). General adsorption conditions: pH = 7, solid to liquid ratio (S/L) = 1 g L^{-1}, T = 25 °C.

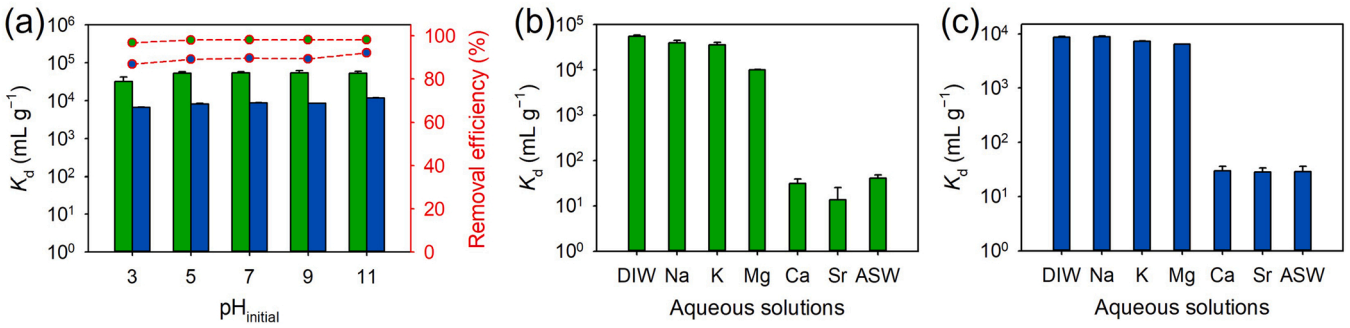

Fig. 3. (a) K_d^{Cs} and R^{Cs} for KMP and NMP at various initial pH values. Effect of coexisting ions on K_d^{Cs} by (b) KMP and (c) NMP (coexisting cations = 10 mM). General adsorption conditions: pH = 7, $C_o \cong 500$ mg L^{-1} (3.76 mM), $t_{KMP} = 240$ min, $t_{NMP} = 1440$ min, $S/L = 1$ g L^{-1}, $T = 25$ °C, green: KMP, blue: NMP.

was 3, the K_d of KMP and NMP slightly decreased to 3.2×10^4 and 6.7×10^3 mL g^{-1}, respectively, owing to the competition between positively charged hydrogen ions and Cs^+ ions on the adsorbent surface. When the pH was 11, the K_d of KMP remained at 5.3×10^4 mL g^{-1}, whereas the K_d value of NMP increased slightly to 1.2×10^4 mL g^{-1}, which is discussed in Section 4.2.1. Additionally, KMP and NMP were stable in the pH range of 3–11, as evidenced by the nearly identical XRD patterns (Fig. S4).

Popular cations, such as Na^+, K^+, Mg^{2+}, Ca^{2+}, and Sr^{2+} may cause competitive adsorption for the removal of Cs^+. As shown in Fig. 3**(b)** and **(c)**, in the presence of Na^+ and K^+, the K_d values of KMP for Cs^+ ranged from 3.5×10^4 mL g^{-1} to 3.9×10^4 mL g^{-1}, whereas those of NMP for Cs^+ were maintained at 7.3×10^3 mL g^{-1} to 8.8×10^3 mL g^{-1}. When Mg^{2+} was present, the K_d values of KMP and NMP to Cs^+ were 9.9×10^3 mL g^{-1} and 6.4×10^3 mL g^{-1}, respectively. In particular, Ca^{2+} and Sr^{2+} had a more substantial effect than other coexisting ions (Na^+, K^+, and Mg^{2+}) and the K_d values of KMP and NMP were 31 mL g^{-1} and 30 mL g^{-1} for Ca^{2+}, respectively. The reasons for this are discussed in

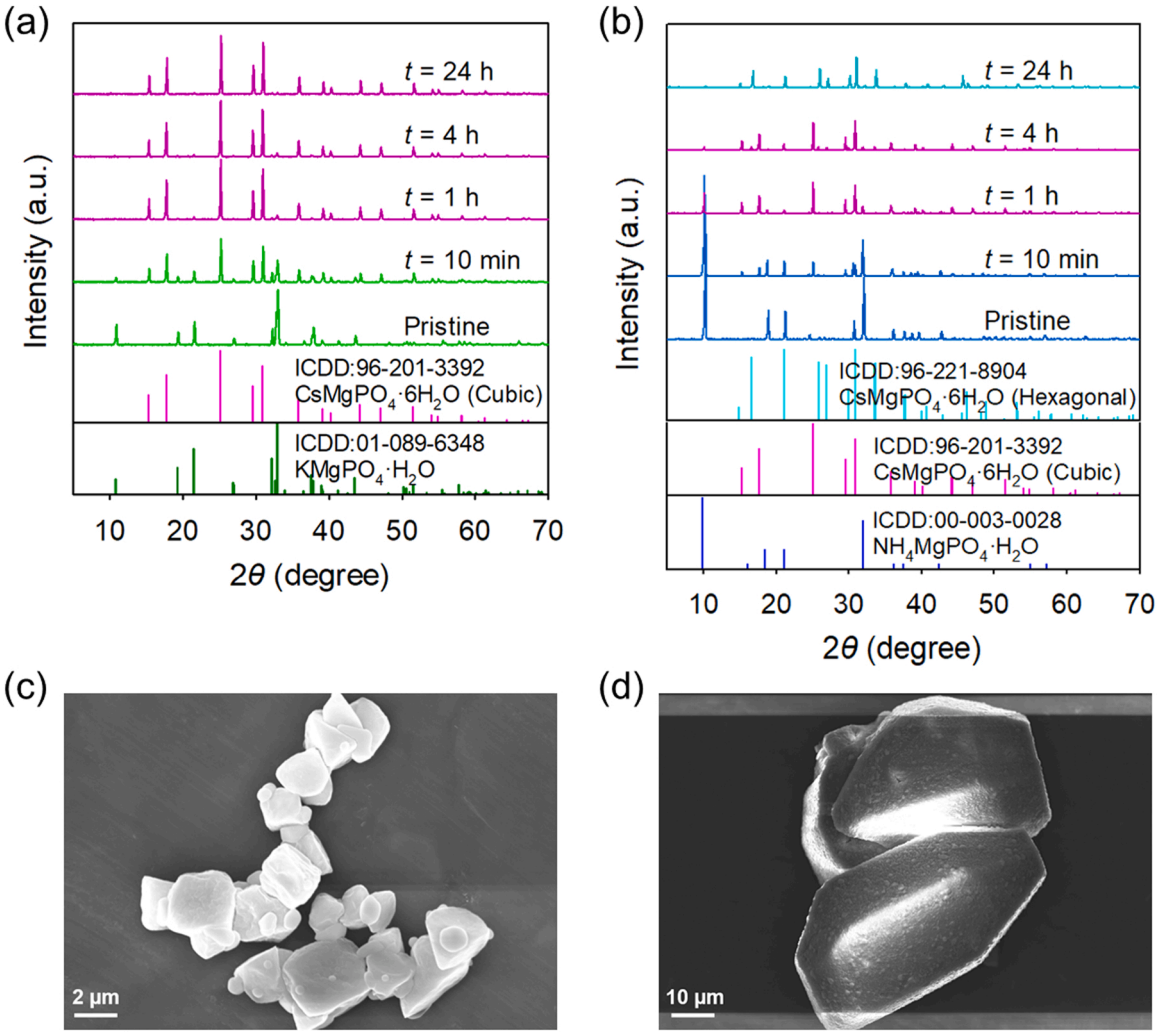

Fig. 4. XRD patterns of (a) KMP and (b) NMP prepared at various adsorption times with Cs^+. FE-SEM images of (c) $CsMP_{cubic}$ and (d) $CsMP_{hexagonal}$. General adsorption conditions: pH = 7, $C_o \cong 1000$ mg L^{-1}, $S/L = 1$ g L^{-1}, $T = 25$ °C.

Section 4.1.1. To evaluate the application of KMP and NMP in real water systems, the distribution coefficient of Cs^+-spiked artificial seawater (ASW) was examined (ion concentrations are shown in Table S1). The K_d values of KMP and NMP in seawater were 41 mL g^{-1} and 29 mL g^{-1}, respectively, which were similar to those in the Ca^{2+} solution. Generally, coexisting cations inhibited the adsorption of KMP and NMP on Cs^+ in the following order: $Ca^{2+}/Sr^{2+} >> Mg^{2+} > K^+/Na^+$.

3.3. Structural transformations of KMP and NMP

The structures of KMP and NMP were investigated using XRD during the Cs^+ adsorption process. Fig. 4**(a)** illustrates that KMP underwent a structural transformation to struvite-type, cubic-structured $CsMgPO_4{\cdot}6H_2O$ ($CsMP_{cubic}$, ICDD: 96–201–3392) in approximately 1 h. On the other hand, NMP (Fig. 4**(b)**) underwent two structural transformations during the adsorption process: first from NMP to $CsMP_{cubic}$ and then to struvite-type, hexagonal-structured $CsMgPO_4{\cdot}6H_2O$ ($CsMP_{hexagonal}$, ICDD: 96–221–8904); The two structures had different arrangements of close-packed layers (Fig. S6**(a)** and **(b)**), which suggests that NH_4^+ in NMP may contribute to the structural transformation of $CsMP_{cubic}$ to $CsMP_{hexagonal}$. The reasons for this are discussed in Section 4.2. FTIR analysis (Fig. S5) also demonstrated the formation of struvite-type CsMPs where the intense peak of the products at 976 cm^{-1} corresponded to the antisymmetric vibration of PO_4^{3-} in struvite [4]. Morphology analysis (Fig. 4**(c)** and **(d)**) showed that $CsMP_{Cubic}$ exhibited a tetrahedral appearance (~3 μm), whereas $CsMP_{hexagonal}$ exhibited a coffin-like appearance (~40 μm).

4. Discussion

4.1. Adsorption processes

4.1.1. Adsorption mechanism

To elucidate the adsorption behavior of Cs^+ on KMP and NMP, the experimental data were evaluated using energy-dispersive X-ray spectroscopy (EDS) mapping and inductively Coupled Plasma Optical Emission spectroscopy (ICP-OES). EDS mapping confirmed that $CsMP_{cubic}$ and $CsMP_{hexagonal}$ were composed of Cs, Mg, P, and O (Fig. S7 **(c, d)**). The $CsMP_{cubic}$ and $CsMP_{hexagonal}$ samples revealed a homogeneous distribution of Cs, whereas K and N were much lower than those of KMP and NMP (Fig. S7**(a, b)**), suggesting that Cs^+ was exchanged with K^+ or NH_4^+. To further confirm the ion exchange ratio of K^+ to Cs^+ during the adsorption of Cs^+ by KMP, 20 mg of KMP crystals was immersed in 20 mL of 1000 mg L^{-1} Cs^+ solution, and the concentrations of Cs^+, K^+, and Mg^{2+} were monitored at different stages throughout the adsorption process. As shown in Fig. 5**(a)** and Table S4, the concentration of K^+ in the solution increased and stabilized at 3.532 mmol g^{-1} (62.3 %) as the concentration of Cs^+ in the solution decreased, whereas the Mg^{2+} in the solution remained at a negligible concentration. According to correlation analysis, the increase in the amount of K^+ was positively correlated with a decrease in the amount of Cs^+ in the solution (Fig. 5**(b)**). The obtained slope was 0.814, which indicates that the desorption of 0.814 mol K^+ occurred during the adsorption of 1 mol Cs^+. These results indicate that K^+ in KMP and Cs^+ in the solution engaged in an ion-exchange process. However, the actual amount of K^+ desorbed was less than the theoretical value.

As shown in Fig. 4, the structure and size of the post-adsorption products changed. To verify the dissolution of KMP, 20 mg of KMP powder was added to 20 mL of deionized water. As shown in Fig. 5**(a)** and Table S4, the concentrations of K^+ and Mg^{2+} increased rapidly during the first 30 min and reached equilibrium at ~2 h. The concentrations of K^+ and Mg^{2+} in the solution increased to 0.378 mmol g^{-1} and 0.465 mmol g^{-1} at 4 h, accounting for 6.66 % and 8.19 % of the total K and Mg contents in the KMP adsorbent, respectively. This indicated that KMP was partially dissolved in water, and the dissolved Mg^{2+} and PO_4^{3-} may form CsMPs when combined with H_2O and Cs^+. Previous studies have suggested that Cs^+ tends to accumulate on the surface of the particles as struvite when heterogeneous precipitation is performed [24,31, 55]. While Cs^+ underwent ion exchange with K^+, some of the Cs^+ formed CsMPs with Mg and P on the KMP surface, which explains why the slope of the fitted equation was less than 1. Thus, it can be concluded that ion exchange and dissolution-precipitation are concurrent processes, with the former being dominant. Because NMP has a structure similar to that of KMP, it has the same adsorption mechanism.

The adsorption of Cs^+ on KMP and NMP is primarily driven by electrostatic interactions and struvite formation. Divalent ions such as Sr^{2+}, Ca^{2+} and Mg^{2+} affected the adsorption of Cs^+ due to their electrostatic interactions (Fig. 3**(b)** and **(c)**). The formation of struvite also plays a crucial role in Cs^+ adsorption. The significant difference between Sr^{2+}/Ca^{2+} and Mg^{2+} on Cs^+ adsorption explains the effect of struvite formation. Sr^{2+} and Ca^{2+} prevent the formation of struvite [13], which can contain Cs^+ in its structure. Monovalent cations do not prevent the struvite formation and not accommodate in struvite resulting in no competing with Cs^+.

4.1.2. Comparison of Cs^+ adsorption onto dittmarite-type compounds and other adsorbents

The theoretical ion-exchange capacities of the adsorbents were calculated and compared with their actual capacities. The theoretical ion exchange capacity of KMP ($q_{theoretical}^{KMP}$ = 754 mg g^{-1}) was lower than that of NMP ($q_{theoretical}^{NMP}$ = 856 mg g^{-1}) because NH_4^+ has a lower molar weight than K^+; the ion exchange capacities of both NH_4^+ and K^+ were

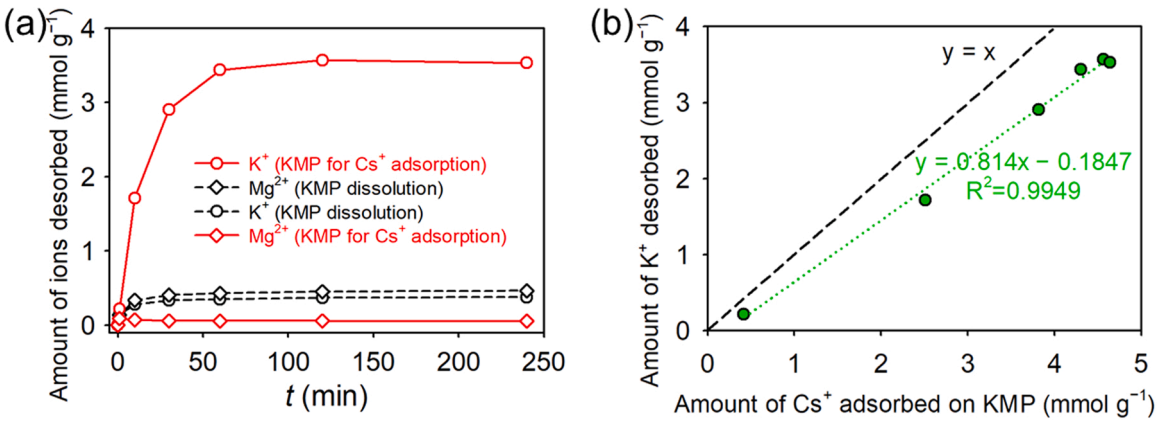

Fig. 5. (a) Variation of K^+ and Mg^{2+} concentrations over time during adsorption and dissolution. (b) Quantitative relationship between the amount of Cs^+ adsorbed onto KMP and K^+ desorbed from KMP. The dashed black line represents a line with a slope of 1. Specific adsorption conditions: pH = 7, $C_o \cong$ 1000 mg L^{-1}. General conditions: S/L = 1 g L^{-1}, T = 25 °C.

higher than that of AMP ($q_{theoretical}^{AMP}$ = 213 mg g^{-1}) and similar to that of α-ZrP and γ-ZrP ($q_{theoretical}^{\alpha-ZrP}$ = 882 mg g^{-1}, $q_{theoretical}^{\gamma-ZrP}$ = 833 mg g^{-1}). We also compared the actual adsorption capacities of the adsorbents in Fig. 6. We observed that the highest q_e values of KMP (630 mg g^{-1}) and NMP (711 mg g^{-1}) for Cs^+ were the highest among previously reported values, including PBIL-BF_4 (592 mg g^{-1}) [7], InSnOS (532 mg g^{-1}) [56], and Zeolite-Rho (497 mg g^{-1}) [26]. The highest q_e values of γ-ZrP [8], AMP-PAN [40], and α-ZrP [39] were 225, 83, and 64 mg g^{-1}, respectively, which were much lower than the theoretical q because AMP is not layered and ZrP has H as an interchangeable ion, which is affected by the dissociation constant and additional hydrogen bonding. Because KMP and NMP had high q_e, they are good candidates for minimizing the volume of radioactive wastewater containing Cs^+.

The K_d values of KMP and NMP were compared with those of previously reported adsorbents (Table S5). KMP had a higher K_d for Cs^+ than NMP, ZIF-8-FC [25], InSnOS [56], FJSM-SnS [43], and AMP-PAN [40] but lower than KAlSnS-3 [58], 3D rGO/PBAs [18], and KTS-3 [45].

The adsorption of Sr^{2+} and Co^{2+}, which can also exist in wastewater from nuclear power plants, was also tested. NMP showed a high q_e value of 529 mg g^{-1} for Co^{2+} and a low q_e value of 107 mg g^{-1} for Sr^{2+}. KMP showed low q_e values of 109 and 140 mg g^{-1} for both Co^{2+} and Sr^{2+} (Fig. S8). The high q_e value of NMP for Co^{2+} was likely because of the smaller ionic radius of Co^{2+} (0.65 Å) than that of Sr^{2+} (1.18 Å) and the larger ionic radius of NH_4^+ (1.48 Å [49]) than that of K^+ (1.38 Å [48]).

4.2. Mechanisms of the $CsMP_{hexagonal}$ / $CsMP_{cubic}$ polymorph switch

4.2.1. Mechanism of influence of interlayer ions on pH

Generally, pH is one of the main factors controlling the struvite morphology, size, and growth rate [34,42]. At pH 7, KMP and NMP produced $CsMP_{cubic}$ and $CsMP_{hexagonal}$, respectively (Fig. 4). To examine the change in the pH during Cs^+ adsorption, a pH meter was used to measure the pH of the solution. As shown in Fig. 7**(a)**, the initial pH of the solutions was 7, and after 10 min, the pH values of both solutions increased, most likely because of the reaction of the negatively charged surfaces of KMP and NMP with H_2O to form OH^- (Eq. 4**)**. In addition, the partial dissolution of the adsorbent released PO_4^{3-} into water. Because the phosphate species (PO_4^{3-}, HPO_4^{2-}, $H_2PO_4^-$) coexisted in different percentages at different pH values (Fig. S9**(a)**), PO_4^{3-} reacted with H_2O to form HPO_4^{2-} and OH^- (Eq. 5**)** [9]. After 10 min, the pH of the KMP and NMP solutions decreased and stabilized at 9.0 and 8.4, respectively. The pH of the solution after the adsorption of Cs^+ by NMP was significantly lower than that of the solution after the adsorption of Cs^+ by KMP, owing to the presence of NH_4^+. In Fig. S9**(b)**, when the pH of the solution was higher than 7, NH_4^+ reacted with OH^- in the solution to generate $NH_{3(aq)}$ and H_2O, causing a decrease in the pH of the solution (Eq. 6**)** [28].

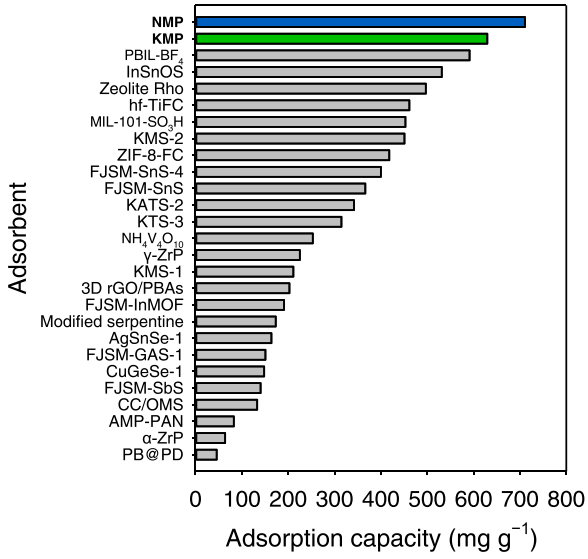

Fig. 6. Comparison of the highest q_e values of various adsorbents for Cs^+. Some data were estimated using WebPlotDigitizer (ver. 4.5). PBIL-BF_4 [7], InSnOS [56], Zeolite-Rho [26], hf-TiFC [59], MIL-101-SO_3H [1], KMS-2 [36], ZIF-8-FC [25], FJSM-SnS-4 [27], FJSM-SnS [43], KATS-2 [57], KTS-3 [45], $NH_4V_4O_{10}$ [61], γ-ZrP [8], KMS-1 [33], 3D rGO/PBAs [18], FJSM-InMOF [15], Modified serpentine [31], AgSnSe-1 [12], FJSM-GAS-1 [14], CuGeSe-1 [32], FJSM-SbS [30], CC/OMS [10], AMP-PAN [40], α-ZrP [39], and PB@PD [60].

$$\equiv PO^-_{(s)} + H_2O \rightarrow \equiv POH_{(s)} + OH^- \quad (4)$$

$$PO_4^{3-} + H_2O \rightarrow HPO_4^{2-} + OH^- \quad (5)$$

$$NH_4^+{}_{(aq)} + OH^- \rightarrow NH_{3(aq)} + H_2O \quad (6)$$

The improved adsorption performance of NMP at pH = 11 (Fig. 3**(a)**) can be explained by that the high concentration of OH^- promoted the positive direction of Eq. 6 and subsequent additional ion exchange between NH_4^+ in NMP and Cs^+ in solution.

4.2.2. Variation in pH and structural transformation

To determine the relationship between pH and structural transformation, the relationship between the pre-adsorption pH ($pH_{initial}$) and post-adsorption pH (pH_{final}) of KMP and NMP in the Cs^+ solution was determined (Fig. 7**(b)**). The products of KMP and NMP after Cs^+ adsorption under different initial pH conditions were characterized using XRD (Fig. 7**(c)** and Fig. 7**(d)**). When the initial pH was 3, the final pH after the adsorption of Cs^+ by KMP and NMP changeed to 7.9 and 8.0 (Fig. 7**(b)** and Fig. S10**(a)**), respectively, and their products were transformed into $CsMP_{hexagonal}$. When the initial pH was 5–9, the pH of the KMP and NMP solutions finally stabilized at 9.5 and 8.5, which indicated that KMP and NMP had buffering capacities in the initial pH range of 5–9. The XRD patterns in these pH ranges indicated that the products of KMP and NMP were $CsMP_{cubic}$ and $CaMP_{hexagonal}$, respectively. When the initial pH of the solution was further increased to 11, the final pH after Cs^+ adsorption by KMP remained almost constant (pH_{final} = 10.9). In contrast, the final pH value at equilibrium after adsorption by NMP decreased to 8.7 **(**Fig. S10**(b))**. The XRD patterns showed that both the KMP and NMP adsorption products were transformed into $CsMP_{cubic}$. The transformation from $CsMP_{cubic}$ to $CsMP_{hexagonal}$ for NMP at pH 7 (Fig. 4**(b)**) was caused by a change in pH (Fig. 7**(a)**). In summary, when the pH of the solution was lower than 8.6, KMP and NMP tended to transform into $CsMP_{hexagonal}$ and when it was higher than 8.6, they tended to transform into $CsMP_{cubic}$ (Fig. 7**(b)** and **S11**). Further studies will be required to analyze the phosphate state and structure of CsMPs under different solution pH conditions.

5. Conclusions

An adsorbent with a high adsorption capacity has the advantage of reducing the volume of radioactive waste. Two dittmarite-type magnesium phosphates, KMP and NMP, were successfully synthesized and used to remove Cs^+ from aqueous solutions. The highest q_e values of KMP and NMP measured experimentally were 630 mg g^{-1} and 711 mg g^{-1}, respectively, which are the highest among any reported adsorbents. The combination of ion exchange and dissolution-precipitation contributed to the high adsorption capabilities of KMP and NMP, which were close to their theoretical values. While KMP and NMP may not be suitable for use in waters with high divalent ion concentrations, they can still be used in readsorption processes, following desorption processes, to concentrate Cs^+ and reduce waste volume. Additionally, the reduced waste will be stable after vitrification or immobilization. In conclusion, the high adsorption capacity and stability of KMP and NMP make them promising candidates for the treatment of radioactive wastewater. This study not only provides valuable information on the properties and mechanisms of

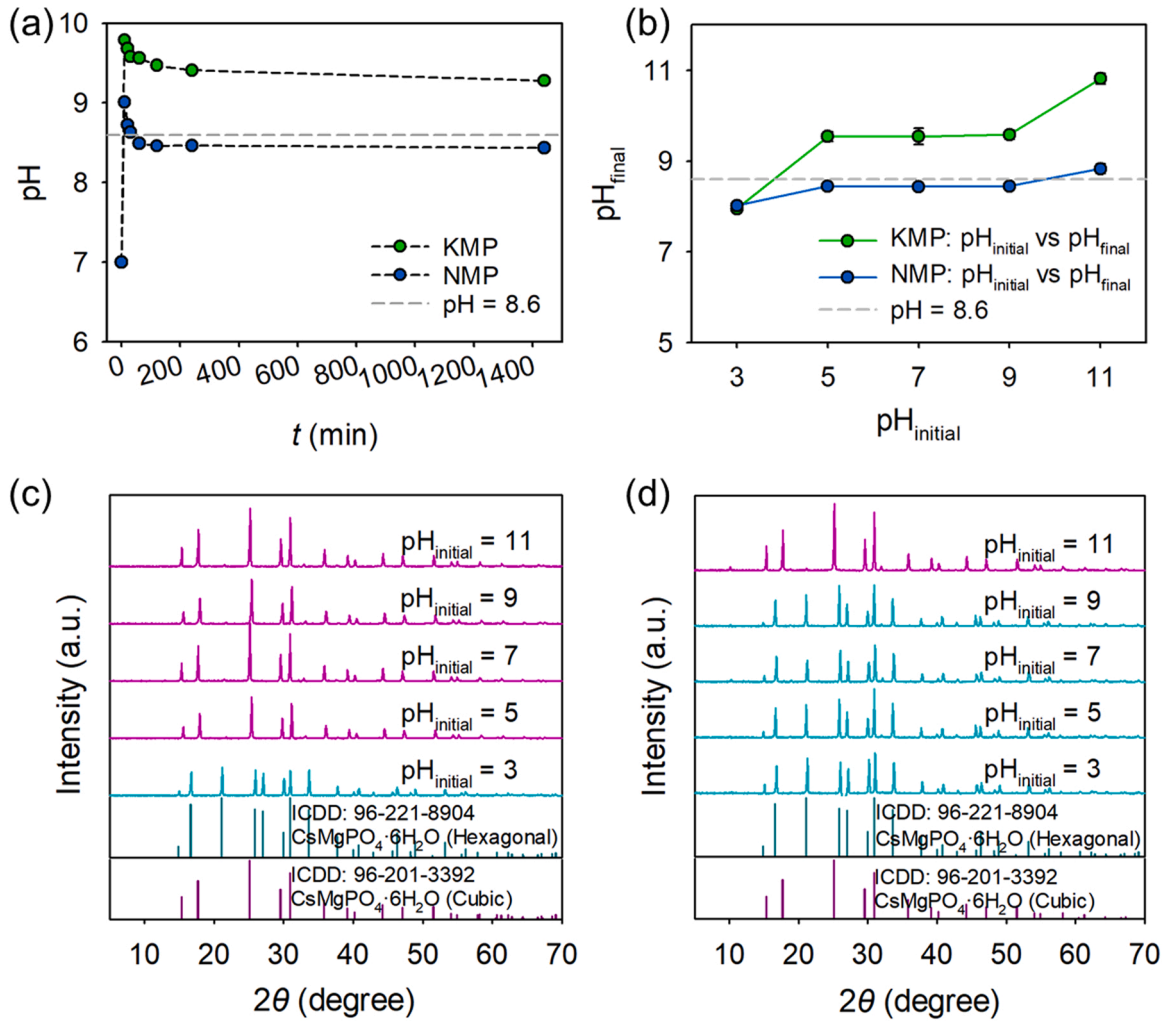

Fig. 7. (a) pH changes over time for KMP and NMP at initial pH of 7; (b) Plot of final pH versus initial pH of KMP and NMP with Cs^+ solution. XRD patterns of (c) KMP and (d) NMP after Cs^+ adsorption at different initial pH. General adsorption conditions: $C_o \cong 1000$ mg L^{-1}, $t = 1440$ min, $S/L = 1.0$ g L^{-1}, $T = 25$ °C.

dittmarite-type magnesium phosphates as Cs^+ adsorbents, but also contributes to the development of efficient and cost-effective methods for the disposal of radioactive waste.

CRediT authorship contribution statement

Zeqiu Li: Conceptualization, Investigation, Visualization, Writing-Original draft.

Chenyang Yang: Investigation, Validation.

Kuk Cho: Conceptualization, Validation, Writing- Review and Editing, Supervision.

Declaration of Competing Interest

The authors declare that they have no known competing financial interests or personal relationships that could have appeared to influence the work reported in this paper.

Data availability

Data will be made available on request.

Acknowledgements

This work was supported by the National Research Foundation (NRF) grant funded by the Ministry of Education, Republic of Korea [2020R1A6A1A03044834; 2022R1I1A3063150].

Appendix A. Supporting information

Supplementary data associated with this article can be found in the online version at doi:10.1016/j.jhazmat.2023.131385.

References

[1] Aguila, B., Banerjee, D., Nie, Z., Shin, Y., Ma, S., Thallapally, P.K., 2016. Selective removal of cesium and strontium using porous frameworks from high level nuclear waste. Chem Commun 52, 5940–5942. https://doi.org/10.1039/C6CC00843G.

[2] Alby, D., Charnay, C., Heran, M., Prelot, B., Zajac, J., 2018. Recent developments in nanostructured inorganic materials for sorption of cesium and strontium: synthesis and shaping, sorption capacity, mechanisms, and selectivity—a review. J Hazard Mater 344, 511–530. https://doi.org/10.1016/j.jhazmat.2017.10.047.

[3] Bai, Z., Hu, C.-L., Liu, L., Zhang, L., Huang, Y., Yuan, F., Lin, Z., 2019. $KMg(H_2O)PO_4$: a deep-ultraviolet transparent nonlinear optical material derived from $KTiOPO_4$. Chem Mater 31, 9540–9545. https://doi.org/10.1021/acs.chemmater.9b03950.

[4] Banks, E., Chianelli, R., Korenstein, R., 1975. Crystal chemistry of struvite analogs of the type $MgMPO_4{\cdot}6H_2O$ ($M^+ = K^+$, Rb^+, Cs^+, Tl^+, NH_4^+). Inorg Chem 14, 1634–1639. https://doi.org/10.1021/ic50149a041.

[5] Bryan, G.W., 2009. The accumulation of ^{137}Cs by brackish water invertebrates and its relation to the regulation of potassium and sodium. J Mar Biol Assoc United Kingdom 43, 541–565. https://doi.org/10.1017/S0025315400000503.

[6] Carling, S.G., Day, P., Vissen, D., 1995. Crystal and magnetic structures of layer transition metal phosphate hydrates. Inorg Chem 34, 3917–3927. https://doi.org/10.1021/ic00119a013.

[7] Chen, S., Dong, Y., Wang, H., Sun, J., Wang, J., Zhang, S., Dong, H., 2022. Highly efficient and selective cesium recovery from natural brine resources using mesoporous Prussian blue analogs synthesized by ionic liquid-assisted strategy. Resour, Conserv Recycl 186, 106542. https://doi.org/10.1016/j.resconrec.2022.106542.

[8] Cheng, Y., Dong Wang, X., Jaenicke, S., Chuah, G.-K., 2018. Mechanochemistry-based synthesis of highly crystalline γ-zirconium phosphate for selective ion exchange. Inorg Chem 57, 4370–4378. https://doi.org/10.1021/acs.inorgchem.7b03202.

[9] Conrad, J., Tremaine, P.R., 2021. Third dissociation constant of phosphoric acid in H_2O and D_2O from 75 to 300°C at p=20.4 MPa using Raman spectroscopy and a titanium-sapphire flow cell. Phys Chem Chem Phys 23, 10670–10685. https://doi.org/10.1039/D0CP06266A.

[10] Dai, Y., Lv, R., Fan, J., Peng, H., Zhang, Z., Cao, X., Liu, Y., 2020. Highly ordered macroporous silica dioxide framework embedded with supramolecular as robust recognition agent for removal of cesium. J Hazard Mater 391, 121467. https://doi.org/10.1016/j.jhazmat.2019.121467.

[11] Ding, D., Zhang, Z., Chen, R., Cai, T., 2017. Selective removal of cesium by ammonium molybdophosphate – polyacrylonitrile bead and membrane. J Hazard Mater 324, 753–761. https://doi.org/10.1016/j.jhazmat.2016.11.054.

[12] Ding, D., Cheng, L., Wang, K.-Y., Liu, H.-W., Sun, M., Wang, C., 2020. Efficient Cs^+–Sr^{2+} separation over a microporous silver selenidostannate synthesized in deep eutectic solvent. Inorg Chem 59, 9638–9647. https://doi.org/10.1021/acs.inorgchem.0c00770.

[13] Enyemadze, I., Momade, F.W.Y., Oduro-Kwarteng, S., Essandoh, H., 2021. Phosphorus recovery by struvite precipitation: a review of the impact of calcium on struvite quality. J Water, Sanit Hyg Dev 11, 706–718. https://doi.org/10.2166/washdev.2021.078.

[14] Feng, M.-L., Sarma, D., Gao, Y.-J., Qi, X.-H., Li, W.-A., Huang, X.-Y., Kanatzidis, M. G., 2018. Efficient Removal of $[UO_2]^{2+}$, Cs^+, and Sr^{2+} ions by radiation-resistant gallium thioantimonates. J Am Chem Soc 140, 11133–11140. https://doi.org/10.1021/jacs.8b07457.

[15] Gao, Y.-J., Feng, M.-L., Zhang, B., Wu, Z.-F., Song, Y., Huang, X.-Y., 2018. An easily synthesized microporous framework material for the selective capture of radioactive Cs^+ and Sr^{2+} ions. J Mater Chem A 6, 3967–3976. https://doi.org/10.1039/C7TA11208D.

[16] Hashimoto, S., Komatsu, M., Miura, S., 2022. In: Radioactive Materials Released by the Fukushima Nuclear Accident. Forest Radioecology in Fukushima: Radiocesium Dynamics, Impact, and Future. Springer Nature Singapore, Singapore, pp. 1–10. https://doi.org/10.1007/978-981-16-9404-2_1.

[17] Haynes, W.M., 2016. CRC handbook of chemistry and physics, 97th ed.,. CRC press,, Boca Raton.

[18] Huo, J., Yu, G., Wang, J., 2021. Selective adsorption of cesium (I) from water by Prussian blue analogues anchored on 3D reduced graphene oxide aerogel. Sci Total Environ 761, 143286. https://doi.org/10.1016/j.scitotenv.2020.143286.

[19] Ji, Y.-Y., Ochi, K., Hong, S.B., Nakama, S., Sanada, Y., Mikami, S., 2021. Performance of in situ gamma-ray spectrometry in the assessment of radioactive cesium deposition around the Fukushima Daiichi nuclear power plant. Radiat Phys Chem 179, 109205. https://doi.org/10.1016/j.radphyschem.2020.109205.

[20] Koleva, V., Zhecheva, E., Stoyanova, R., 2011. Facile synthesis of $LiMnPO_4$ olivines with a plate-like morphology from a dittmarite-type $KMnPO_4{\cdot}H_2O$ precursor. Dalton Trans 40, 7385–7394. https://doi.org/10.1039/C1DT10515A.

[21] Koleva, V.G., 2005. Metal–water interactions and hydrogen bonding in dittmarite-type compounds $M'M''PO_4{\cdot}H_2O$ ($M'=K^+$, NH_4^+; $M''=Mn^{2+}$, Co^{2+}, Ni^{2+}): correlations of IR spectroscopic and structural data. Spectrochim Acta Part A: Mol Biomol Spectrosc 62, 1196–1202. https://doi.org/10.1016/j.saa.2005.04.025.

[22] Koleva, V.G., Boyadzhieva, T.J., Stoyanova, R.K., 2019. Crystal and morphology design of dittmarite-type ammonium iron–manganese phosphates, $NH_4Mn_{1-x}Fe_xPO_4{\cdot}H_2O$, as precursors for phospho-olivine electrodes. Cryst Growth Des 19, 3744–3754. https://doi.org/10.1021/acs.cgd.9b00094.

[23] Komarneni, S., Roy, R., 1982. Use of γ-zirconium phosphate for Cs removal from radioactive waste. Nature 299, 707–708. https://doi.org/10.1038/299707a0.

[24] Kononenko, O.A., Milyutin, V.V., Makarenkov, V.I., Kozlitin, E.A., 2021. Immobilization of NPP evaporator bottom high salt-bearing liquid radioactive waste into struvite-based phosphate matrices. J Hazard Mater 416, 125902. https://doi.org/10.1016/j.jhazmat.2021.125902.

[25] Le, Q.T.N., Cho, K., 2021. Caesium adsorption on a zeolitic imidazolate framework (ZIF-8) functionalized by ferrocyanide. J Colloid Interface Sci 581, 741–750. https://doi.org/10.1016/j.jcis.2020.08.017.

[26] Lee, H.Y., Kim, H.S., Jeong, H.-K., Park, M., Chung, D.-Y., Lee, K.-Y., Lee, E.-H., Lim, W.T., 2017. Selective removal of radioactive cesium from nuclear waste by zeolites: on the origin of cesium selectivity revealed by systematic crystallographic studies. J Phys Chem C 121, 10594–10608. https://doi.org/10.1021/acs.jpcc.7b02432.

[27] Li, J., Jin, J., Zhang, T., Ma, W., Zeng, X., Sun, H., Cheng, M., Feng, M., Huang, X., 2021. Rapid and selective uptake of Cs^+ and Sr^{2+} ions by a layered thiostannate with acid–base and irradiation resistances. ACS ES&T Water 1, 2440–2449. https://doi.org/10.1021/acsestwater.1c00290.

[28] Li, L., Lollar, B.S., Li, H., Wortmann, U.G., Lacrampe-Couloume, G., 2012. Ammonium stability and nitrogen isotope fractionations for $–NH_3(aq)–NH_3(gas)$ systems at 20–70°C and pH of 2–13: Applications to habitability and nitrogen cycling in low-temperature hydrothermal systems. Geochim Cosmochim Acta 84, 280–296. https://doi.org/10.1016/j.gca.2012.01.040.

[29] Li, Z., Vivas, E.L., Yang, C., Suh, Y.J., Cho, K., 2022. Layered potassium calcium phosphate with multiple exchangeable cations for Sr(II) and Co(II) removal from water. Sep Purif Technol 299, 121789. https://doi.org/10.1016/j.seppur.2022.121789.

[30] Liao, Y.-Y., Li, J.-R., Zhang, B., Sun, H.-Y., Ma, W., Jin, J.-C., Feng, M.-L., Huang, X.-Y., 2021. Robust and flexible thioantimonate materials for Cs^+ remediation with distinctive structural transformation: a clear insight into the ion-exchange mechanism. ACS Appl Mater Interfaces 13, 5275–5283. https://doi.org/10.1021/acsami.0c21756.

[31] Liu, B., Yu, S., Ye, Y., Zhang, Q., Lei, Z., Liu, X., 2018. Enhanced cesium removal through heterogeneous chemical precipitation on modified magnesium silicate mineral. Acta Microsc 27, 269–278.

[32] Liu, H.-W., Wang, K.-Y., Ding, D., Sun, M., Cheng, L., Wang, C., 2019. Deep eutectic solvothermal synthesis of an open framework copper selenidogermanate with pH-resistant Cs^+ ion exchange properties. Chem Commun 55, 13884–13887. https://doi.org/10.1039/C9CC06906B.

[33] Manos, M.J., Kanatzidis, M.G., 2009. Highly efficient and rapid Cs^+ uptake by the layered metal sulfide $K_{2x}Mn_xSn_{3-x}S_6$ (KMS-1). J Am Chem Soc 131, 6599–6607. https://doi.org/10.1021/ja900977p.

[34] Matynia, A., Koralewska, J., Wierzbowska, B., Piotrowski, K., 2006. The influence of process parameters on struvite continuous crystallization kinetics. Chem Eng Commun 193, 160–176. https://doi.org/10.1080/009864490949008.

[35] Melnikov, P., Zanoni, L.Z., 2010. Clinical effects of cesium intake. Biol Trace Elem Res 135, 1–9. https://doi.org/10.1007/s12011-009-8486-7.

[36] Mertz, J.L., Fard, Z.H., Malliakas, C.D., Manos, M.J., Kanatzidis, M.G., 2013. Selective removal of Cs^+, Sr^{2+}, and Ni^{2+} by $K_{2x}MgxSn_{3-x}S_6$ (x = 0.5–1) (KMS-2) relevant to nuclear waste remediation. Chem Mater 25, 2116–2127. https://doi.org/10.1021/cm400699r.

[37] Momma, K., Izumi, F., 2008. VESTA: a three-dimensional visualization system for electronic and structural analysis. J Appl Crystallogr 41, 653–658. https://doi.org/10.1107/S0021889808012016.

[38] Mu, W., Chen, B., Yu, Q., Li, X., Wei, H., Yang, Y., Peng, S., 2021. A novel zirconium phosphonate adsorbent for highly efficient radioactive cesium removal. J Mol Liq 326, 115307. https://doi.org/10.1016/j.molliq.2021.115307.

[39] Mu, W., Yu, Q., Chen, B., Li, X., Wei, H., Yang, Y., Peng, S., 2021. Effect of guest molecules on the adsorption properties of intercalated α-ZrP for Sr^{2+} and Cs^+. J Mol Liq 323, 114585. https://doi.org/10.1016/j.molliq.2020.114585.

[40] Park, Y., Lee, Y.-C., Shin, W.S., Choi, S.-J., 2010. Removal of cobalt, strontium and cesium from radioactive laundry wastewater by ammonium molybdophosphate–polyacrylonitrile (AMP–PAN). Chem Eng J 162, 685–695 doi:10.1016/j.cej.2010.06.026.

[41] Priyadharsini, N., Shanmugavani, A., Vasylechko, L., Kalai Selvan, R., 2018. Sol-gel synthesis, structural refinement, and electrochemical properties of potassium manganese phosphate for supercapacitors. Ionics 24, 2073–2082 doi:10.1007/s11581-018-2449-y.

[42] Prywer, J., Torzewska, A., Płociński, T., 2012. Unique surface and internal structure of struvite crystals formed by Proteus mirabilis. Urol Res 40, 699–707. https://doi.org/10.1007/s00240-012-0501-3.

[43] Qi, X.-H., Du, K.-Z., Feng, M.-L., Li, J.-R., Du, C.-F., Zhang, B., Huang, X.-Y., 2015. A two-dimensionally microporous thiostannate with superior Cs^+ and Sr^{2+} ion-exchange property. J Mater Chem A 3, 5665–5673. https://doi.org/10.1039/C5TA00566C.

[44] Raju, K., 2020. Ammonium metal phosphates: emerging materials for energy storage. Curr Opin Electrochem 21, 351–357. https://doi.org/10.1016/j.coelec.2020.03.019.

[45] Sarma, D., Malliakas, C.D., Subrahmanyam, K., Islam, S.M., Kanatzidis, M.G., 2016. $K_{2x}Sn_{4-x}S_{8-x}$(x= 0.65–1): a new metal sulfide for rapid and selective removal of Cs^+, Sr^{2+} and UO_2^{2+} ions. Chem Sci 7, 1121–1132. https://doi.org/10.1039/C5SC03040D.

[46] Sasaki, K., Tsuruyama, S., Moriyama, S., Handley-Sidhu, S., Renshaw, J.C., Macaskie, L.E., 2012. Ion exchange capacity of Sr^{2+} onto calcined biological hydroxyapatite and implications for use in permeable reactive barriers. Mater Trans 53, 1267–1272. https://doi.org/10.2320/matertrans.M-M2012813.

[47] Schlenz, H., Neumeier, S., Hirsch, A., Peters, L., Roth, G., 2018. Phosphates as safe containers for radionuclides. In: Soraya, H.-A., Georg, A., Melanie, J. (Eds.), Highlights in Applied Mineralogy. De Gruyter, Berlin, Boston, pp. 171–196. https://doi.org/10.1515/9783110497342-009.

[48] Shannon, R.D., 1976. Revised effective ionic radii and systematic studies of interatomie distances in halides and chaleogenides. Acta Crystallogr A32, 751–767. https://doi.org/10.1107/S0567739476001551.

[49] Sidey, V., 2016. On the effective ionic radii for ammonium. Acta Crystallogr B72, 626–633. https://doi.org/10.1107/S2052520616008064.

[50] Šoptrajanov, B., Stefov, V., Kuzmanovski, I., Jovanovski, G., Lutz, H.D., Engelen, B., 2002. Very low H–O–H bending frequencies. IV. Fourier transform infrared spectra of synthetic dittmarite. J Mol Struct 613, 7–14. https://doi.org/10.1016/S0022-2860(02)00136-9.

[51] Svendsen, E.R., Kolpakov, I.E., Karmaus, W.J., Mohr, L.C., Vdovenko, V.Y., McMahon, D.M., Jelin, B.A., Stepanova, Y.I., 2015. Reduced lung function in children associated with cesium 137 body burden. Ann Am Thorac Soc 12, 1050–1057. https://doi.org/10.1513/AnnalsATS.201409-432OC.

[52] Tan, Y., Sha, L., Yu, N., Yang, Z., Qu, J., Xu, Z., 2020. Mechanochemical approach to synthesize citric acid-soluble fertilizer of dittmarite ($NH_4MgPO_4{\cdot}H_2O$) from talc/$NH_4H_2PO_4$ mixture. RSC Adv 10, 17686–17693. https://doi.org/10.1039/D0RA00387E.

[53] Torre-Fernández, L., Trobajo, C., de Pedro, I., Alfonso, B.F., Fabelo, O., Blanco, J. A., García, J.R., García-Granda, S., 2013. Ammonium–cobalt–nickel phosphates, $NH_4[Co_{1-x}Ni_xPO_4]{\cdot}H_2O$. J Solid State Chem 206, 75–84. https://doi.org/10.1016/j.jssc.2013.07.039.

[54] Villars, P., 2012. $NH_4MgPO_4{\cdot}H_2O$ ($[NH_4]Mg[PO_4][H_2O]$) Crystal Structure: Datasheet from "PAULING FILE Multinaries Edition. SpringerMaterials, (https://materials.springer.com/isp/crystallographic/docs/sd_1400160), in, Springer-Verlag GmbH, Heidelberg, 2012.
[55] Wagh, A.S., Sayenko, S., Shkuropatenko, V., Tarasov, R., Dykiy, M., Svitlychniy, Y., Virych, V., Ulybkina, E, 2016. Experimental study on cesium immobilization in struvite structures. J Hazard Mater 302, 241–249. https://doi.org/10.1016/j.jhazmat.2015.09.049.
[56] Wang, L., Pei, H., Sarma, D., Zhang, X.-M., MacRenaris, K., Malliakas, C.D., Kanatzidis, M.G., 2019. Highly selective radioactive $^{137}Cs^+$ capture in an open-framework oxysulfide based on supertetrahedral cluster. Chem Mater 31, 1628–1634. https://doi.org/10.1021/acs.chemmater.8b04877.
[57] Yang, C., Cho, K., 2021. Rapid and selective removal of Cs^+ from water by layered potassium antimony thiostannate. J Hazard Mater 403, 124105. https://doi.org/10.1016/j.jhazmat.2020.124105.
[58] Yang, C., Suh, Y.J., Cho, K., 2022. Highly selective cesium removal under acidic and alkaline conditions using a novel potassium aluminum thiostannate. Chemosphere 301, 134610 doi:10.1016/j.chemosphere.2022.134610.
[59] Yang, H.-M., Park, C.W., Kim, I., Yoon, I.-H., 2020. Hollow flower-like titanium ferrocyanide structure for the highly efficient removal of radioactive cesium from water. Chem Eng J 392, 123713. https://doi.org/10.1016/j.cej.2019.123713.
[60] Yoon, S., Choi, M., Hwang, Y., Bae, S., 2021. Upcycling of steel slag for manufacture of Prussian-blue-encapsulated pectin beads and its use for efficient removal of aqueous cesium. J Clean Prod 319, 128786. https://doi.org/10.1016/j.jclepro.2021.128786.
[61] Zhang, H., Li, C., Chen, X., Fu, H., Chen, Y., Ning, S., Fujita, T., Wei, Y., Wang, X., 2022. Layered ammonium vanadate nanobelt as efficient adsorbents for removal of Sr^{2+} and Cs^+ from contaminated water. J Colloid Interface Sci 615, 110–123. https://doi.org/10.1016/j.jcis.2022.01.164.
[62] Zhenyu, L., Jueshi, Q., Zhongyuan, L., Qian, L., Qiulin, Z., 2012. Rapid synthesis of dittmarite by microwave-assisted hydrothermal method. Adv Mater Sci Eng 2012, 968396. https://doi.org/10.1155/2012/968396.